MTLA 38 (2024) 102233

Contents lists available at ScienceDirect

Materialia

journal homepage: www.elsevier.com/locate/mtla

Compressive behavior of SLA open-cell lattices: A comparison between triply periodic minimal surface gyroid and stochastic structures for artificial bone

Miguel Araya [a,b,*], Josué Murillo [a], Rafael Vindas [c], Teodolito Guillén [a]

[a] Bio-inspired Processes and Materials Research Group, Instituto Tecnológico de Costa Rica, Cartago, 30101, Costa Rica
[b] School of Industrial Design, Tecnológico de Costa Rica, Cartago, 30101, Costa Rica
[c] School of Veterinary Medicine, Universidad Nacional de Costa Rica, Heredia, 40104, Costa Rica

ARTICLE INFO

Keywords:
Open-cell lattices
TPMS gyroid
Stochastic
Stereolithography (SLA)
Compressive properties
Artificial bone

ABSTRACT

This study evaluates the compressive properties of stereolithography (SLA) fabricated open-cell lattices, specifically triply periodic minimal surface (TPMS) gyroid and stochastic structures, for artificial bone applications. Two resins, Standard White and BioMed Amber, were tested across four relative densities (0.2, 0.3, 0.4, 0.5). Mechanical characterization of horse tuber coxae trabecular bone used as a biological comparator showed an average elastic modulus of 0.05 GPa and a yield strength of 3.369 MPa. Gyroid structures exhibited higher elastic modulus and yield strengths, with BioMed Amber gyroid at a density of 0.5, achieving an elastic modulus of 0.623 GPa and yield strength of 14.149 MPa. Stochastic structures showed lower and more variable mechanical properties. The highest yield strength for stochastic structures was observed in BioMed Amber at a density of 0.5 (14.199 MPa). Comparative analysis indicated that high-performing synthetic structures approach the lower bounds of natural bone properties. Using a field-driven design approach, variable relative density structures were developed to emulate the mechanical properties of natural bone. SEM analysis provided insights into failure mechanisms, highlighting the impact of relative density on structural integrity and material ductility. This research supports the development of 3D-printed bone-like structures as viable substitutes for cadaveric specimens in preclinical tests, with implications for material science and orthopedic applications.

1. Introduction

Nature's architectures, such as bone, combine intricate geometries with outstanding functional properties, presenting significant challenges for traditional prototyping methods. Additive Manufacturing (AM) has revolutionized the ability to replicate these complex structures, transforming rapid manufacturing processes and significantly impacting the biomedical manufacturing sector. The improved quality of the parts in this industry has progressively become more complex, where the applications of AM technologies are being rapidly enhanced to become more important in the biomedical manufacturing industry. Notably, bone tissue engineering created a path to printing porous scaffolds with engineered chemically controlled direct and interconnected porosity topologies [1–5]. AM technologies take advantage of several parameters in the creation of complex internal structures [1,2,6,7], which makes them techniques with the potential to replicate the mechanical properties of bone [8,9] by controlling the internal architecture structure and porosity density [3,10–14]. These technologies offer a wide range of possibilities in the 3D printing field. Geometric complexity makes fabrication and product customization possible. The extended range of materials used in AM technologies widened to include polymers, ceramics, and metals [6,15]. Thus, AM has pushed the topologically complex structures to be part of the biomedical industry at various levels of length scales, from the nanoscale to the macroscale [16]. The advances allow design for additive manufacturing (DfAM) to vary several properties in complex morphological lattices compared to the bulk material, enabling multi-functionality. This makes customization easier and enhances the design capabilities [17–19].

Materials with purposefully designed structures can achieve tailored mechanical properties and specific functionalities [20–22]. In the

* Corresponding author at: Bio-inspired Processes and Materials Research Group, Instituto Tecnológico de Costa Rica, Cartago, 30101, Costa Rica.
E-mail addresses: miaraya@itcr.ac.cr (M. Araya), josuedmr0@estudiantec.cr (J. Murillo), rafael.vindas.bolanos@una.cr (R. Vindas), tguillen@itcr.ac.cr (T. Guillén).

https://doi.org/10.1016/j.mtla.2024.102233
Received 25 June 2024; Accepted 10 September 2024
Available online 11 September 2024

medical sector, one of the applications is biomimicry, in which it is possible through AM technologies to imitate properties of natural structures and tissues such as bones, muscles, and tendons, among others [2,6,7,23–26]. Here, Triply Periodic Minimal Surface (TPMS) and stochastic structures are designed to integrate with living tissues and serve as standalone bone models that exhibit similar biomechanical behaviors to human bone. These models offer a pathway toward eliminating the variabilities associated with cadaveric samples, providing more consistent and controlled environments for biomechanical testing. TPMS, such as gyroid structures, are recognized for their minimal surface area and excellent load-bearing properties, which distribute stress evenly. The gyroid structure is characterized by its continuous, non-self-intersecting, and periodic nature. It is known for its high specific strength and unique geometric properties, and the gyroid structure is widely used in applications that require lightweight yet strong materials. Its complex, curved surfaces also contribute to excellent mechanical performance, including enhanced energy absorption and fatigue resistance, making it a popular choice in biomaterials and advanced manufacturing fields [27,28]. These characteristics make them highly suitable for biomedical applications, where they mimic trabecular bone's geometric and mechanical properties [29–31]. Compared to TPMSs, stochastic structures are more suitable for providing closer mimicry to native bone. These structures use a random point process where a family of points is distributed in each space known, where statistical (e.g., Poisson-Voronoi process) and mathematical functions are used to create a lattice structure from a random set [16,32,33].

Previous research shows the application of additive manufacturing technologies for designing and developing cellular scaffolds in orthopedic implant applications. [6,34,35], becoming an ideal tool to obtain the optimal internal architecture of porous implants that satisfy functional requirements and bio-mimic human bone [2,5,7,14,34,36]. These approaches show the potential of using AM technologies and computer-aided design and engineering (CAD-CAE) tools to develop artificial bone for biomechanical assessments of medical devices in the laboratory. The trabecular bone has a cellular structure. Architecturally, it is formed by a connected network of rods and plates, extended in different directions defined by the orientation of major stress within the bone [37]. Polymeric foams can imitate mechanical behavior in other cellular materials. Knowing the deformation mechanisms in such materials has led to understanding how their mechanical properties depend on their relative density, wall properties, and cell geometry [38,39]. Relative density is the density of the cellular solid divided by that of the solid from which it is made and is equivalent to the volume fraction of the solid [40]. In practice, the relative density of trabecular bone ranges from about 0.05 to 0.5 (i.e., any bone with a relative density less than 0.7 is classified as trabecular) [38].

The theoretical framework provided by L.J. Gibson on the mechanical behavior of cellular materials informs the design of these synthetic bones, modeling them to mimic the compression behavior of trabecular bone across three regimes: linear elasticity, stress plateau, and densification [40]. Understanding these models is crucial for engineering synthetic bones that behave like their natural counterparts, particularly in how they respond under biomechanical stress, primarily through buckling in low-density regions [40].

The primary goal of this study is to develop and validate synthetic bone models using stereolithography (SLA) open-cell lattices, with a focus on TPMS gyroid and stochastic structures, to replace cadaveric bone in preclinical biomechanical tests. By leveraging AM technologies, this research aims to produce synthetic bones that closely mimic human trabecular bone's mechanical properties and offer standardization and reproducibility in testing environments. The approach includes a detailed examination of the influence of various design parameters and material choices on the mechanical properties of the printed structures. Through rigorous testing and comparative analysis, the study seeks to identify optimal configurations that achieve the closest match to the biomechanical characteristics of natural bone, thereby enhancing the reliability and relevance of preclinical laboratory testing.

2. Materials and methods

2.1. Statistical methodology

To evaluate the factors that may influence the compressive properties of SLA open cell structures, a Design of Experiment (DoE) was conducted as a statistical method. The analyzed factors were the specimen's material with two levels, open-cell type with two levels, and the relative density (RD) with four levels in a multilevel factorial design with 3 replicates, for a total of 48 runs. Materials studied were Formlabs (Formlabs, Somerville, MA, USA) SLA Standard White and BioMed Amber resins. Table 1 displays the constitutive properties of the resins, as provided by the manufacturer datasheets.

Open-cell types studied were a Gyroid walled Triple Periodical Minimal Surfaces (TPMS) and a Voronoi Volume Lattice with stochastic structure constructed by random points in space. TPMS Gyroid and Stochastic lattice were digitally designed using implicit modeling with CAD software nTopology (nTopology, New York, NY, USA). Eq. (1) describes the surface of TPMS Gyroid, where a and t control unit cell size and porosity, respectively [41].

$$\theta(x,y,z)_{Gyroid} = \sin\left(\frac{2\pi}{a}x\right)cos\left(\frac{2\pi}{a}y\right) + \sin\left(\frac{2\pi}{a}y\right)cos\left(\frac{2\pi}{a}z\right) + sin\left(\frac{2\pi}{a}z\right)cos\left(\frac{2\pi}{a}x\right) = t \quad (1)$$

The Stochastic structure is based on a random point process, typically a Poisson-Voronoi process, where a set of seed points P_i are distributed randomly in the space. Each seed point generates a cell V_i, defined in Eq. (2):

$$V_i = \left\{x \in \mathbb{R}^3 \mid \| x - P_i \| \leq \| x - P_j \| \ \forall j \neq i\right\} \quad (2)$$

This equation defines a region where any point x within the region V_i is closer to the seed point P_i than to any other seed point P_j. The strut thickness and the average spacing between generated points in space are controlled parameters to manipulate the relative density of the Voronoid structure.

RD was controlled by setting the design variables: "strut thickness" and "cell size" for TPMS and "strut thickness" and "the average spacing between generated points in space." CAD-related variables can be visualized in Fig. 1. For statistical analysis, Minitab 22 Statistical software was used.

2.2. Mechanical Testing of horse tuber coxae and synthetic bone

Specimens of the lattice structures for compressive testing were fabricated using Formlabs Form3B (Formlabs, Somerville, MA, USA) SLA 3D printer. The specimen's geometry was created according to ASTM D695–15. The test specimen geometry was created using a computer-aided design (CAD) software nTopology (nTopology, New York, NY, USA) exported as a Standard Triangle Language (STL) and

Table 1
Constitutive properties of the resins.

Post-Cured Resin	Tensile Modulus (GPa)	Ultimate Tensile Strength (MPa)	Elongation	Method
Standard White	2.8	65	6 %	ASTM D638–10
BioMed Amber	2.9	73	12 %	ASTM D638–10

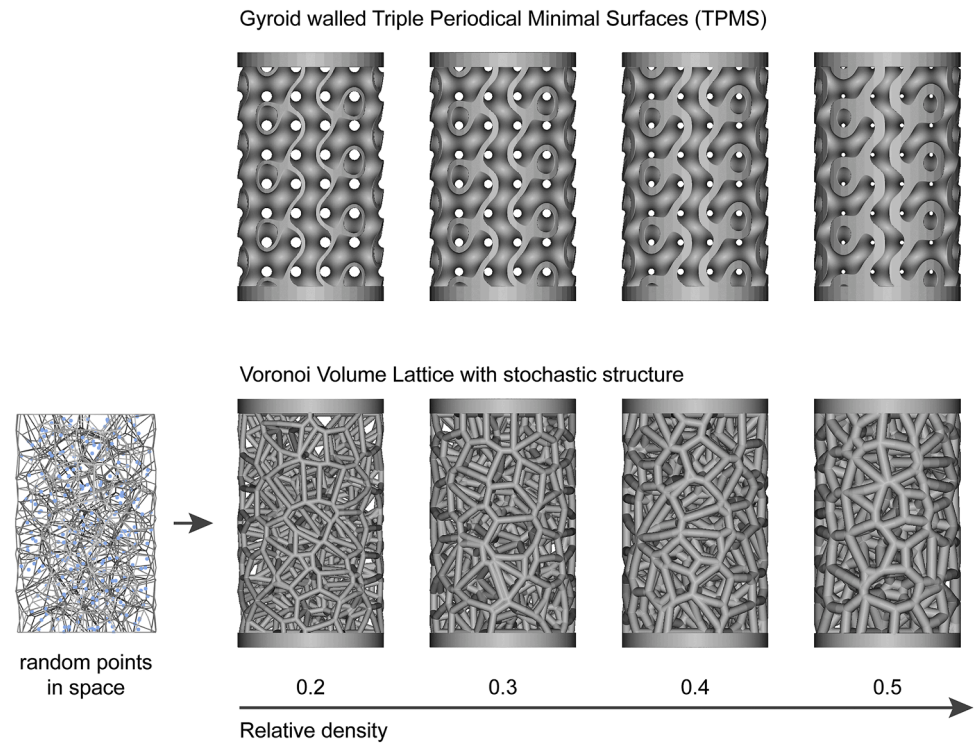

Fig. 1. Set of open-cell structure types and relative density selected for the study. The set is composed of two open-cell structures (TPMS, Voronoi Volume Lattice stochastic) and four different relative densities (0.2, 0.3, 0.4, 0.5).

imported into the slicing software Preform (Formlabs, Somerville, MA, USA) to set the printing variables and fabricate them. All specimens were printed "stand" on the print platform, with a layer print high of 50 μm. Following fabrication, the specimens printed with Standard White resin underwent a post-processing procedure that began with a 10-min wash in isopropyl alcohol under constant agitation to ensure thorough cleaning. After washing, the specimens were subjected to a UV and heat treatment at 60 °C for 30 min, optimizing their mechanical strength and stability. A similar post-processing protocol was applied to the Biomed Amber resin specimens, adjusting to accommodate the material's specific requirements. These specimens were washed for 20 min in isopropyl alcohol, ensuring complete removal of any residuals. They were then exposed to UV light and heat at 70 °C for 60 min, which enhanced their structural integrity and material properties.

Six samples were extracted from horse cadaveric tuber coxae for mechanical examination. The samples were extracted from the cadaveric bone using a 12.5 mm trephine drill. Fig. 2 shows the sample preparation process.

Both tuber coxae and SLA lattice samples were tested using an MTS Bionix Universal Machine with a 2.5 KN load cell. The compressive strain rate used was 1.3 mm/min. Force–displacement data was used to plot stress-strain curves and calculate the response variables, such as Compressive Young's Modulus and compressive yield strength. Young's modulus was calculated from the slope of the initial, linear portion of the stress-strain curve, where the material exhibits elastic behavior, returning to its original shape upon removal of the applied stress. Yield strength was identified at the point on the stress-strain curve where the material transitions from elastic deformation to permanent (plastic) deformation. The 0.2 % offset method was employed to determine the yield strength.

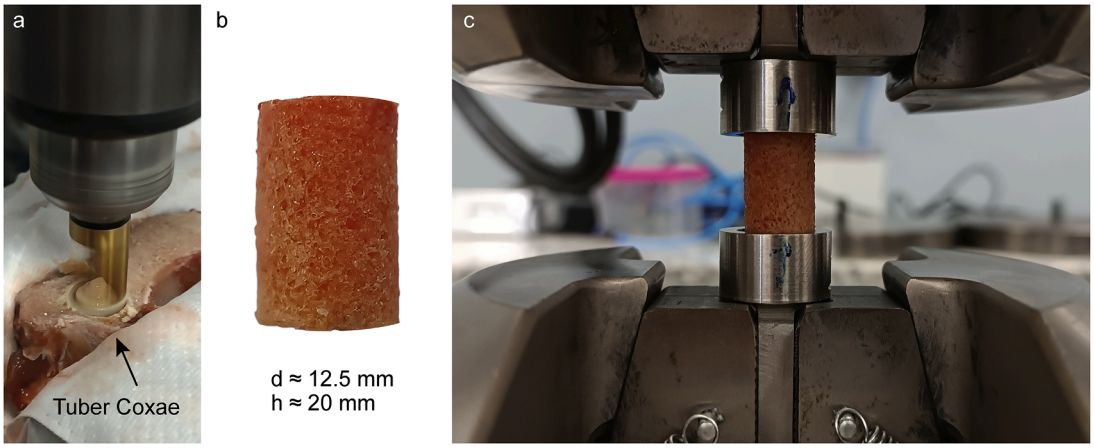

Fig. 2. Tuber coxae sample preparation. Use of trephine to extract cylindrical sample (a). Extracted sample dimensions (b). Compressive test (c).

2.3. Synthetic bone scanning electron microscopy analysis

The specimens used in this study were examined using Scanning Electron Microscopy (SEM). This analysis was performed to identify and verify the internal structure of the 3D-printed samples, characterize SLA technology, and examine the failure mechanism. The specimens were mounted using carbon conducting tape before being sputter-coated with a gold target. A Jeol JSM-6390LV SEM was used at 20 KeV.

2.4. Field driven design to generate bone-like structures

To emulate bone-like structures within a femoral model, the implicit design methodology was employed using the nTopology software (nTopology, New York, NY, USA). Initially, a femoral .obj model was imported into the software. The model underwent a series of refinements, including remeshing to optimize mesh quality, followed by conversion into an implicit format suitable for further manipulations and analyses.

A static finite element analysis (FEA) was conducted to assess the stress distribution within the bone structure. The model was assigned an orthotropic linear elastic material property in accordance with the human bone properties characterized by Li et al. [42] with a density of 2 g/cm^3, detailed properties are tabulated in Table 2. The calculation of the shear modulus G was based on the relationship in the Eq. (3):

$$G = \frac{E}{2(1+\nu)} \tag{3}$$

where E is the Young's modulus and ν is the Poisson's ratio.

Following FEA, topology optimization (TO) was implemented to optimize the material distribution within the model to achieve the best structural performance with the least amount of material. TO was conducted using Structural Compliance Response as the Design Objective to minimize the deformation under loading conditions while respecting a minimum feature constraint of 1 mm. The result is a points map that drives the density distribution, directly influencing the structure's final geometry.

The boundary conditions applied for the simulation included a load of 1000 N vectorially distributed along the x, y, and z axes at the femoral head to simulate natural force distribution during standing or walking. At the base of the femur, a displacement restraint was implemented to mimic the constraint conditions in a physiological setting.

Outputs from the TO were transformed into a scalar point map showing element densities. This map was a critical input for field-driven design, a method grounded in the mathematical framework of fields that define values at every point within a specified space. As elaborated by George Allen [43], a scalar field in this context is a real-valued function defined over a three-dimensional space that assigns numerical values at any given point (x,y,z). A ramp block tool in nTopology was utilized to manipulate the design parameters based on the stress distribution. This tool adjusts field values by rescaling existing fields according to defined input and output thresholds. For instance, if the existing field F(x,y,z) holds values, the Ramp block modifies these values such that:

$$G\ (x,y,z) = b_0 \text{ if } F\ (x,y,z) < a_0 \tag{4}$$

$$G\ (x,y,z) = b_1 \text{ if } F\ (x,y,z) > a_1 \tag{5}$$

For values $a_0 < F\ (x,y,z) < a_1$, G interpolates linearly between b_0 and b_1. Fig. 3 shows graphically the use of a ramp block to generate variable relative density within a lattice structure.

Table 2
Orthotropic linear elastic material properties.

Elastic Modulus	(GPa)	Poisson's Ratio		Shear Modulus	(GPa)
E1	13.00	Nu12	0.3	G12	5.00 GPa
E2	13.00	Nu23	0.3	G23	5.00 GPa
E3	18.00	Nu13	0.3	G13	6.923 GPa

3. Results and discussion

The mechanical properties of horse tuber coxae trabecular bone and synthetic bone lattices produced via SLA with varying densities and materials were evaluated to explore their potential as bone replacement materials.

3.1. Mechanical Characterization of horse tuber coxae trabecular bone

Fig. 4 and Table 3 show the compressive mechanical results of the horse tuber coxae. The average elastic modulus of the horse tuber coxae trabecular bone was 0.05 GPa, and the average yield strength was 3.369 MPa. These values indicate a relatively low stiffness and strength, characteristic of trabecular bone, known for its porous structure. The stress-strain curves evidenced the characteristic mechanical behavior of open-cell structures [38,44], where three regimens are observed: a linear elastic behavior, followed by a plateau with variance in the stress related to collapsing of the struts and, finally, a densification of the structure after the collaboration stage. The samples presented a typical stress-strain curve for stretch-dominated structures, where it is observed to maintain more of a plateau after the linear elastic regime, as the struts yield and collapse prior to densification [45,46].

3.2. Mechanical characterization of SLA lattice structures

The synthetic bone lattices exhibited a broad range of mechanical properties, influenced by both the design (gyroid vs. stochastic) and the material composition (Standard white vs. Biomed amber), as well as the relative density (0.2, 0.3, 0.4, 0.5). Fig. 5 and Table 4 summarize the mechanical results. The gyroid structures generally showed higher values in both elastic modulus and yield strength across all materials and densities, suggesting a more efficient load-bearing architecture than stochastic structures. Specifically, the Biomed amber gyroid with a density of 0.5 exhibited the highest elastic modulus (0.623 GPa) and yield strength (14.149 MPa) among the tested configurations. Regarding rigidity, the Gyroid deforms with behavior dominated by stretching rather than bending, allowing enhanced performance [30,47]. In contrast, the stochastic structures demonstrated generally lower elastic moduli and yield strengths across similar densities and materials. Interestingly, stochastic structures made with Biomed amber showed a disproportionately lower elastic modulus, especially noticeable at lower densities (0.005 GPa at 0.2 density), yet maintained higher yield strengths (e.g., 14.199 MPa at 0.5 density), which might be attributable to the inherent material properties and the random nature of the structure influencing stress distribution [48,49] differently than in the gyroid design. The observed performance of stochastic structures made from Biomed amber material highlights a critical aspect of material science and engineering: the interplay between structure design and material properties. This emphasizes that both the design of the structure and the choice of material independently influence the mechanical behavior of a component [50–52].

Cancellous or trabecular bone in humans, such as that found in the tibia head and vertebra, typically exhibits an elastic modulus ranging from 0.02 GPa to 0.64 GPa, with ultimate strength values between 0.9 MPa and 8.8 MPa [53]. These properties align closely with the mechanical characteristics observed in the horse tuber coxae trabecular bone, which presented an average elastic modulus of 0.05 GPa and a yield strength of 3.369 MPa. The similarity in these values suggests that horse tuber coxae trabecular bone can serve as a reasonable biological analog for human trabecular bone, particularly in studies where human bone samples are not readily available.

The SLA synthetic bone structures, especially the gyroid designs fabricated using Biomed amber material, demonstrated superior mechanical performance compared to both the horse tuber coxae

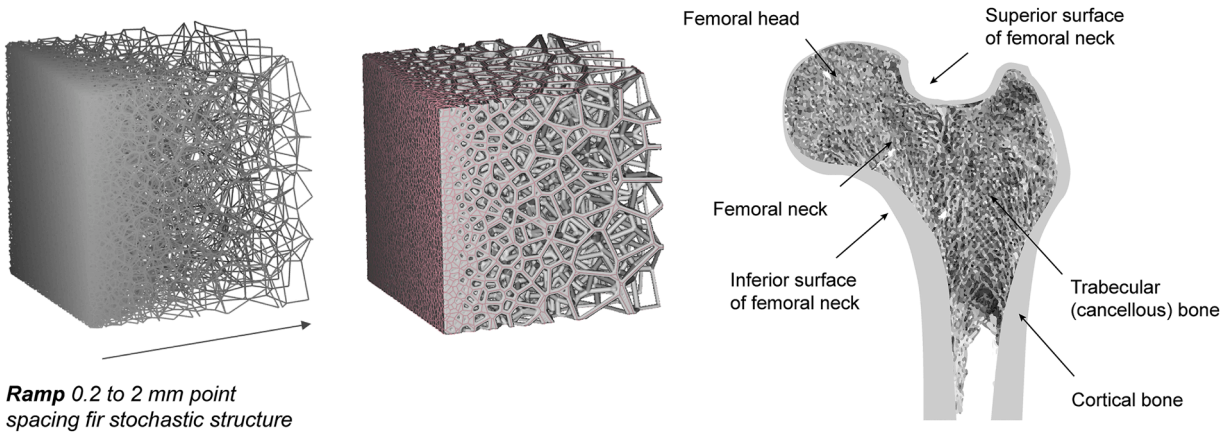

Fig. 3. Synthetic bone design using Stochastic structure with variable Relative Density (left). Anatomy of the human proximal femur (right).

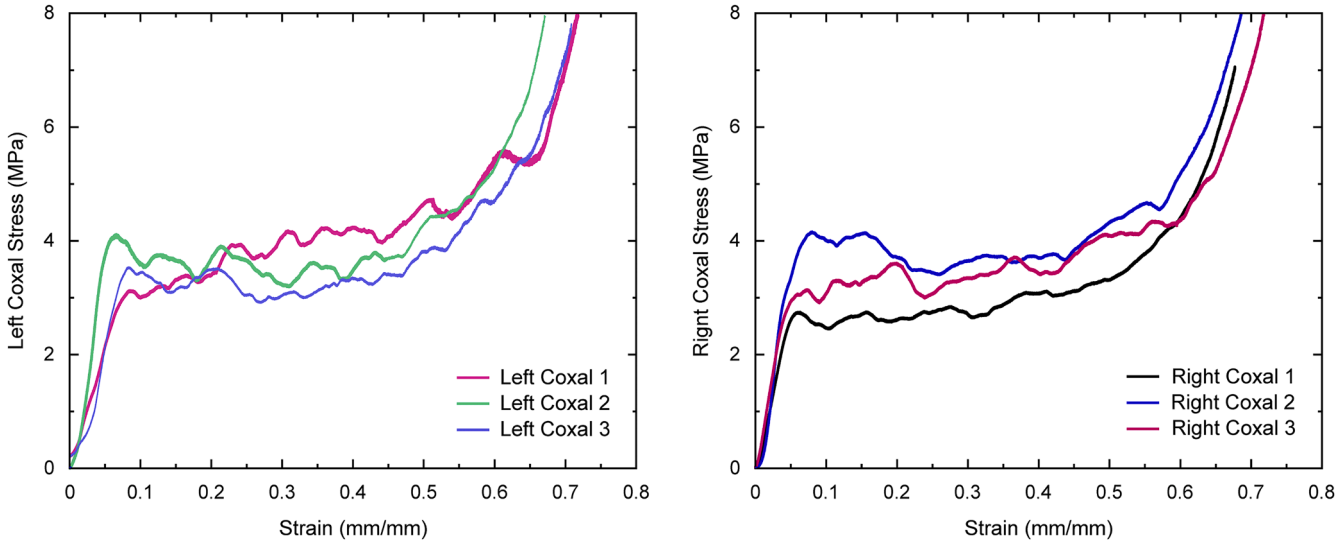

Fig. 4. Stress – strain curves of horse tuber coxae trabecular bone.

Table 3
Average Elastic Modulus and Yield at 0.2 % of Horse Coxae.

Test	Elastic Modulus (GPa)	Yield at 0.2 % (MPa)	Average Elastic Modulus (GPa)	Average Yield at 0.2 % (MPa)
	0.03964	3.02066		
Left Coxa	0.077518	3.7876	0.052	3.409
	0.0386282	3.41961		
	0.050552	2.72698		
Right Coxa	0.047269	4.13143	0.048	3.329
	0.044771	3.12809		

trabecular bone and human trabecular bone. For instance, the gyroid structures with a relative density of 0.5 exhibited an elastic modulus of 0.623 GPa and a yield strength of 14.149 MPa. These values approach the upper range of human trabecular bone's mechanical properties, indicating that these synthetic structures possess sufficient rigidity and strength to support load-bearing applications in bone tissue engineering.

Interestingly, the range of mechanical properties observed in the SLA synthetic bone lattices, particularly the elastic modulus values ranging from 0.005 GPa to 0.623 GPa, can be correlated with cancellous bone from different anatomical parts of the human body [53]. For example, lower density SLA structures, with elastic moduli at the lower end of the range, may resemble the mechanical behavior of cancellous bone found in less load-bearing regions, such as the vertebrae. In contrast, higher density SLA structures with elastic moduli approaching 0.623 GPa are more similar to cancellous bone in load-bearing regions like the femoral head or tibia, where the mechanical demands are greater. This correlation underscores the potential of SLA synthetic lattices to be tailored for specific anatomical applications, depending on the mechanical requirements of the target bone.

The development of 3D-printed bone-like structures using SLA presents a promising avenue for creating synthetic bone models that could replace cadaveric specimens in preclinical tests. The ability to tune the mechanical properties through adjustments in lattice design, material choice, and relative density provides a versatile tool to emulate various bone conditions, ranging from healthy to osteoporotic states. For instance, lower-density stochastic models could simulate weaker bone like those found in osteoporotic patients, whereas higher-density gyroid structures could simulate healthy bone. Moreover, the distinct performance characteristics between the gyroid and stochastic models highlight the potential for selecting specific lattice designs tailored to emulate different anatomical features or pathological conditions of bone. The higher mechanical properties of the gyroid structures suggest their suitability for load-bearing applications. In contrast, the stochastic models, with their unique stress distribution properties, might be better suited for areas where more energy absorption is required. Fig. 6

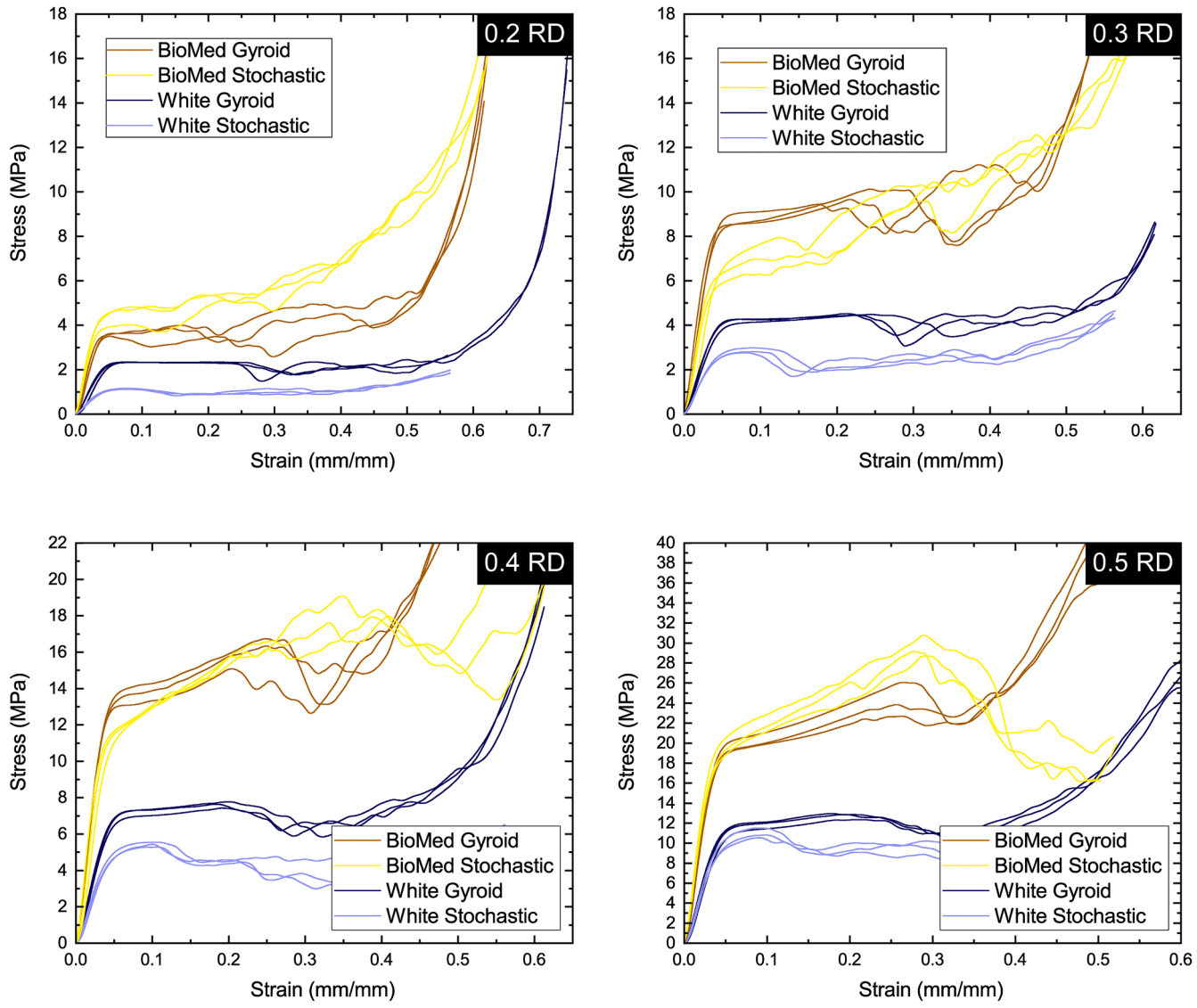

Fig. 5. Stress – Strain curves of lattices fabricated via SLA.

visually compares the response variables, correlating them with the study's factors to facilitate analysis.

Even considering only healthy bone, this is a complex material with non-homogeneous anisotropic properties, especially considering different parts of the bone, age, sex, loading direction or anatomical site. Small changes in geometry can lead to significant variations in its mechanical properties, so multiple variations can be manufactured to take advantage of the characteristics of each structure and configuration. Also, the specific anisotropic properties of different bone types can be artificially generated by choosing the correct topology and applying geometric dilation or density gradients [30,48].

The study of 3D printing of resins is a developing branch, so there are not too many articles that describe and compare resins, which makes its study and future understanding important [54,55]; the BioMed Amber resin shows quite promising results. This material is usually strong and rigid, but its properties can change, as mentioned before. For example, when applying different treatments, in the literature, it is said that when applying artificial aging or polishing, the specimens weaken, showing different behavior in compression and traction tests, which significantly influences the resulting elastic modulus [56].

3.3. Synthetic bone SEM analysis

Fig. 7 presents the SEM images of SLA lattice structures with varying relative densities (RD) in gyroid (0.2–0.5 RD, subfigures a-d) and stochastic (0.2–0.5 RD, subfigures e-h) configurations. The gyroid structures (Fig. 7a-d) show failure predominantly around the mid-sections where the curvature of the triply periodic minimal surfaces (TPMS) alters. Notably, the fractures were both perpendicular and parallel to the manufacturing layer direction, as observed in Fig. 7(a) and (c). In contrast, the stochastic structures (Fig. 7e-h) demonstrated failure occurrences near the nodal points, with fractures predominantly oriented perpendicular to the struts. As the relative density increased across both structures, a decrease in failure cracks was observed, indicating enhanced structural integrity with higher densities.

Fig. 8 provides a detailed view of the failure mechanisms within these structures. SEM analysis reveals significant evidence of lamination failure, evident in Fig. 8(b) and (f) for gyroid and stochastic structures respectively, observable at a magnification that exposes defects smaller than the printing layer resolution. This lamination failure within the material composition extends beyond the typical layer delamination observed in additive manufacturing processes. Fig. 8(c) and (g) present magnified views of delamination within the structures, highlighting that

Table 4
Compressive characterization of lattices fabricated via SLA.

Structure	Material	Relative density (ρ/ρs)	Young Modulus (Gpa)	Yield Strength (MPa)
TPMS Gyroid	Standard White	0.200	0.062 ± 0.002	1.709 ± 0.057
		0.300	0.112 ± 0.005	3.100 ± 0.170
		0.400	0.189 ± 0.002	5.324 ± 0.269
		0.500	0.312 ± 0.009	8.546 ± 0.427
	Biomed Amber	0.200	0.124 ± 0.009	2.839 ± 0.096
		0.300	0.266 ± 0.012	6.564 ± 0.430
		0.400	0.418 ± 0.004	10.131 ± 0.212
		0.500	0.623 ± 0.010	14.149 ± 0.596
Stochastic	Standard White	0.200	0.032 ± 001	0.766 ± 0.032
		0.300	0.079 ± 004	1.898 ± 0.067
		0.400	0.137 ± 0.008	3.701 ± 0.097
		0.500	0.298 ± 0.015	7.477 ± 0.402
	Biomed Amber	0.200	0.005 ± 0.009	3.117 ± 0.252
		0.300	0.006 ± 0.012	4.830 ± 0.366
		0.400	0.014 ± 0.025	8.733 ± 0.118
		0.500	0.020 ± 0.035	14.199 ± 0.714

these defects arise within the material's microstructure rather than from layer separation typically seen in SLA printing. Such findings suggest an inherent failure in the material layer cohesion, potentially increased by the specific material formulation. Additionally, Fig. 8 shows the presence of dimples, as highlighted in Fig. 8(h), suggesting a ductile failure mode. The presence of dimples is noteworthy considering the usually brittle nature of lower-density structures. This observation suggests that the increased relative density enhances the material's toughness, leading to a more ductile failure mechanism.

The SEM analysis elucidates the complex interplay between structure, density, failure, and material integrity in SLA lattice structures, with significant implications for design and processing in additive manufacturing. Increasing the relative density allows the structures to exhibit fewer cracks and improved ductility, crucial for engineering applications demanding high reliability and strength. The evidence of lamination failure also prompts a reevaluation of material choices and processing conditions to mitigate these inherent weaknesses and enhance the mechanical properties of printed structures.

3.4. Synthetic bone through field driven design

Utilizing implicit design, topology optimization, and field-driven design facilitated the creation of femoral head models with TPMS Gyroid lattices. These lattices were tailored using a topology optimization (TO) points map, which was pivotal in driving the design. The models were developed adhering to a design response criterion termed "Structural Compliance Response" and were constrained by a minimum feature size of 1 mm, ensuring structural integrity and manufacturability. Fig. 9 presents the schematic method for developing synthetic bone with variable relative density.

A static FEA was initially performed to evaluate the stress distribution and displacement within the femoral head model under simulated loading conditions. The FEA results revealed a maximum von Mises stress of 25 MPa within the femoral neck area and a maximum total displacement of 1.75 mm at the top part of the femoral head (Fig. 9(c)). The results were consistent when compare with the experimental data observed on cadaveric models by Schileo et al. [57]. These results provided essential insights into potential yielding and deformation within the structure, which were then used as a foundation for the subsequent Single body topology optimization. The optimization process involved 100 iterations, with a design variable count of 49,254, a degree of freedom (DOF) count of 250,707, an element count of 53,474, and a node count of 83,569.

The results from the topology optimization were converted into scalar point map values ranging from 0 to 1, which corresponded to material density distribution across the structure. The topology optimization results were visualized and converted into a scalar point map depicting element densities (Fig. 9(d)). This transformation was crucial for manipulating strut thickness within the lattice structure, which ranged from 0.4 mm to 1 mm. Consequently, this adjustment allowed for a varied computational relative density, spanning from 0.2 to 0.5. These modifications were made using a Ramp Block, which dynamically adjusted the strut thickness based on the density values obtained from the topology optimization, as illustrated in Fig. 9(f).

The variation in lattice thickness and relative density directly influenced the mechanical properties of the models, such as Young's modulus and yield strength, detailed in Table 3. These properties are crucial for simulating different types of bone tissue, ranging from healthy to osteoporotic bone, offering a spectrum of biomechanical behaviors that can be studied in vitro.

4. Conclusions

This study successfully demonstrated the feasibility of using

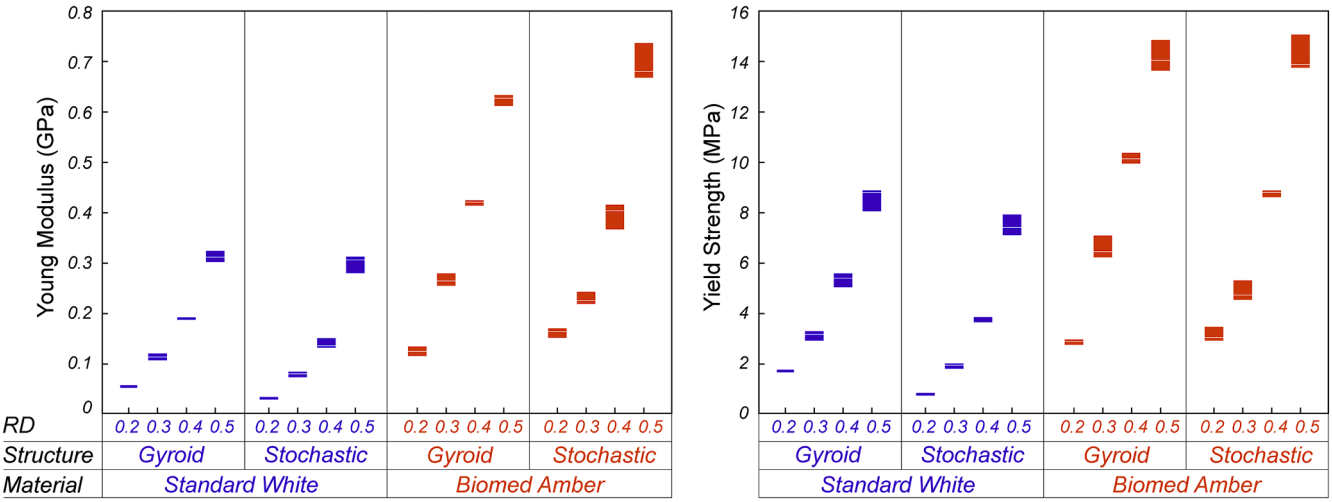

Fig. 6. Elastic Modulus and Yield Strength comparison between the structures.

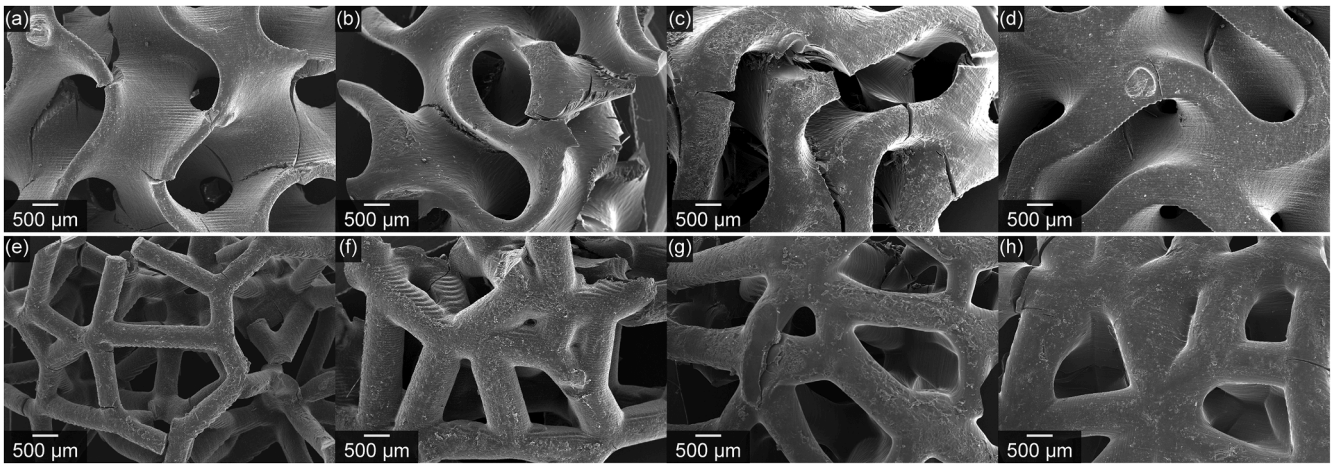

Fig. 7. SEM of SLA lattice structures. Gyroid structure with 0.2 (a), 0.3 (b), 0.4 (c), and 0.5 (d) RD. Stochastic structure with 0.2 (e), 0.3 (f), 0.4 (g), and 0.5 (h) RD.

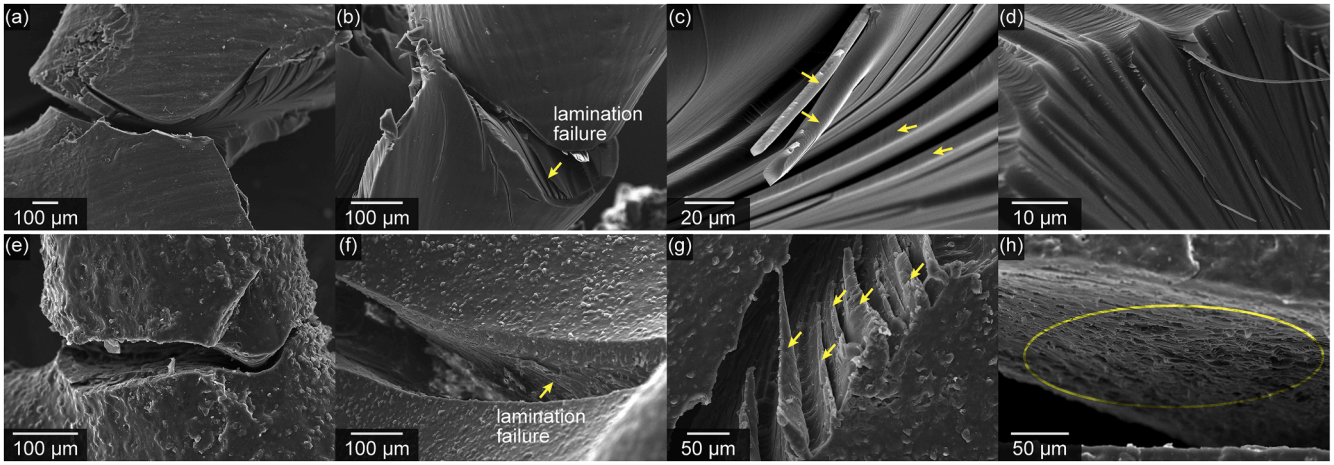

Fig. 8. SEM of SLA lattice structures failure details. Gyroid structure (a) to (d), and Stochastic structure (c) to (h).

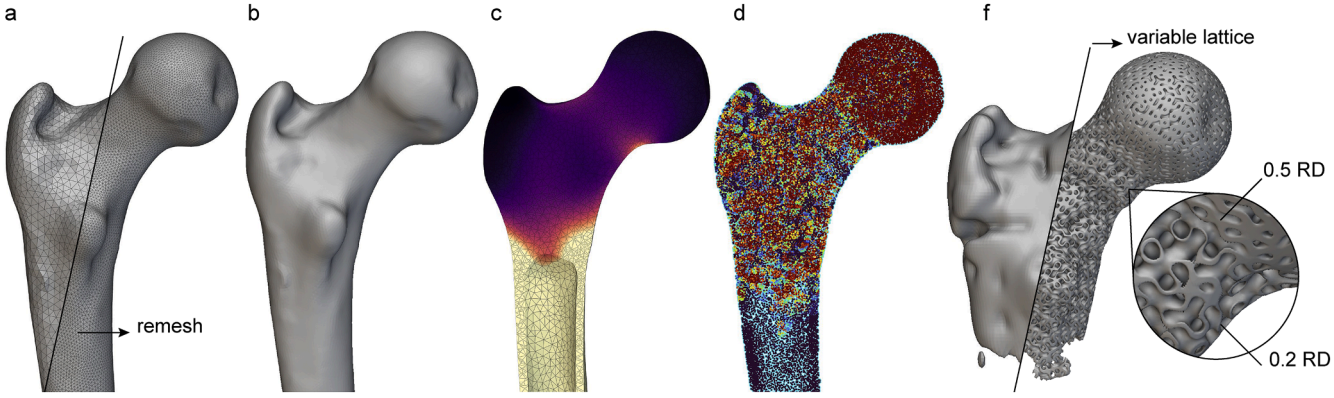

Fig. 9. Synthetic bone design with variable density by using a Ramp Block driven by a Topology Optimization map point Field. Ramesh of .obj femur file (a). Generation of implicit geometry (b). Stress distribution within the model (FEA) (c). Topology Optimization points map (d). TPMS Gyroid variable lattice driven by Topology Optimization points map (f).

stereolithography (SLA) to create synthetic bone models with varying lattice structures and materials that mimic the mechanical properties of natural trabecular bone. Through meticulous testing and analysis, gyroid lattices, especially those fabricated using Biomed Amber resin at higher densities, consistently outperformed stochastic structures in elastic modulus and yield strength, proving their potential for load-bearing orthopedic applications. In contrast, stochastic structures showed variable mechanical properties that could be tuned to mimic weaker bones, such as those affected by osteoporosis, indicating their usefulness in a wide range of biomechanical applications.

The compressive tests on horse tuber coxae trabecular bone and the synthetic lattices revealed critical insights into the behavior of natural

and manufactured structures under load. The superior mechanical performance of the gyroid structures can be attributed to their stretch-dominated deformation, which is beneficial for creating synthetic models that require high stiffness and strength. On the other hand, the stochastic structures, with their unique stress distribution properties, could serve better in applications where energy absorption is crucial.

Moreover, the SEM analyses provided valuable information on the printed lattices' failure mechanisms and structural integrity, underscoring the importance of material choice and lattice design in achieving desired mechanical properties. The ability to adjust lattice thickness and relative density through field-driven design techniques like topology optimization further enhances the potential to tailor synthetic bones for specific anatomical and pathological conditions.

In conclusion, developing SLA-fabricated bone-like structures presents a promising avenue for advancing synthetic models. The ability to precisely control the mechanical properties through design and material choices offers a significant advantage over traditional cadaveric specimens. This approach circumvents the ethical and supply issues associated with human tissues and provides a more consistent and controllable means of conducting preclinical biomechanical tests.

Several challenges must be addressed to translate these findings into real-world clinical applications. One of the primary challenges is ensuring that the synthetic bone materials accurately replicate the complex biomechanical behavior of human cancellous bone under various loading conditions. Additionally, the long-term stability and durability of these synthetic structures must be validated, particularly under cyclic loading, which mimics the repetitive stresses experienced in the human body. The potential variability in mechanical properties due to differences in fabrication processes, could impact the reproducibility of results in laboratory settings. To overcome these challenges, it is essential to conduct extensive validation studies that compare the performance of these synthetic bones with cadaveric samples under a wide range of mechanical tests. Furthermore, advancements in SLA technology, such as the development of new resins and more precise control over lattice architecture, will be crucial in enhancing the reliability and clinical relevance of these synthetic models. Addressing these challenges will pave the way for the broader adoption of AM-fabricated bones in the assessment of medical devices and orthopedic implants, ultimately reducing reliance on cadaveric specimens and improving the consistency and reproducibility of laboratory assessments.

Future work should explore the long-term durability of these materials and structures under cyclic loading conditions to fully validate their potential for clinical application. Moreover, more specific investigations into different AM materials, technologies and their impact on the mechanical properties of the printed structures would be valuable. Additionally, evaluating the performance of these structures under physiological conditions, including exposure to bodily fluids and variable temperature, would provide crucial insights for their clinical translation.

CRediT authorship contribution statement

Miguel Araya: Writing – original draft, Visualization, Validation, Software, Methodology, Investigation, Funding acquisition, Formal analysis, Conceptualization. **Josué Murillo:** Writing – review & editing, Visualization, Formal analysis, Data curation. **Rafael Vindas:** Supervision, Resources, Formal analysis. **Teodolito Guillén:** Writing – review & editing, Supervision, Resources, Project administration, Methodology, Investigation, Funding acquisition, Conceptualization.

Declaration of competing interest

The authors declare that they have no known competing financial interests or personal relationships that could have appeared to influence the work reported in this paper.

Acknowledgments

We express our gratitude to the Research Vice-rectory of Tecnológico de Costa Rica for funding this investigation and the support provided by the Postgraduate Office for this publication. We also thank the National High Technology Center of Costa Rica (CeNAT) for providing the scanning electron microscopy (SEM) images that greatly supported our research.

References

[1] S. Bose, S. Vahabzadeh, A. Bandyopadhyay, Bone tissue engineering using 3D printing, Mater. Today 16 (2013) 496–504, https://doi.org/10.1016/j.mattod.2013.11.017.
[2] A.P. Moreno Madrid, S.M. Vrech, M.A. Sanchez, A.P. Rodriguez, Advances in additive manufacturing for bone tissue engineering scaffolds, Mater. Sci. Eng. C 100 (2019) 631–644, https://doi.org/10.1016/j.msec.2019.03.037.
[3] H. Yin, W. Zhang, L. Zhu, F. Meng, J. Liu, G. Wen, Review on lattice structures for energy absorption properties, Compos. Struct. 304 (2023) 116397, https://doi.org/10.1016/J.COMPSTRUCT.2022.116397.
[4] R. Pugliese, S. Graziosi, Biomimetic scaffolds using triply periodic minimal surface-based porous structures for biomedical applications, SLAS Technol. 28 (2023) 165–182, https://doi.org/10.1016/J.SLAST.2023.04.004.
[5] A. Kalali, H. Rezaie, S. Hesaraki, M. Khodaei, F. Teimoory, A. Saboori, 3D printing of composite scaffolds based on polycaprolactone matrix reinforced with monticellite and akermanite for bone repair; mechanical and biological properties, Materialia (Oxf) 34 (2024) 102057, https://doi.org/10.1016/j.mtla.2024.102057.
[6] X.P. Tan, Y.J. Tan, C.S.L. Chow, S.B. Tor, W.Y. Yeong, Metallic powder-bed based 3D printing of cellular scaffolds for orthopaedic implants: a state-of-the-art review on manufacturing, topological design, mechanical properties and biocompatibility, Mater. Sci. Eng. C 76 (2017) 1328–1343.
[7] A. Nazir, K.M. Abate, A. Kumar, J.Y. Jeng, A state-of-the-art review on types, design, optimization, and additive manufacturing of cellular structures, Int. J. Adv. Manuf. Technol. 104 (2019) 3489–3510, https://doi.org/10.1007/s00170-019-04085-3.
[8] J. Hao, R. Nangunoori, Y.Y. Wu, M. Rajaraman, D. Cook, A. Yu, B. Cheng, K. Shimada, Material characterization and selection for 3D-printed spine models, 3D Print. Med. 4 (2018), https://doi.org/10.1186/s41205-018-0032-9.
[9] M. Tilton, G.S. Lewis, H. Bok Wee, A. Armstrong, M.W. Hast, G. Manogharan, Additive manufacturing of fracture fixation implants: design, material characterization, biomechanical modeling and experimentation, Addit. Manuf. 33 (2020) 101137, https://doi.org/10.1016/j.addma.2020.101137.
[10] S.M. Ahmadi, S.A. Yavari, R. Wauthle, B. Pouran, J. Schrooten, H. Weinans, A. A. Zadpoor, Additively manufactured open-cell porous biomaterials made from six different space-filling unit cells: the mechanical and morphological properties, Materials 8 (2015) 1871–1896, https://doi.org/10.3390/ma8041871.
[11] S.M. Ahmadi, G. Campoli, S. Amin Yavari, B. Sajadi, R. Wauthle, J. Schrooten, H. Weinans, A.A. Zadpoor, Mechanical behavior of regular open-cell porous biomaterials made of diamond lattice unit cells, J. Mech. Behav. Biomed. Mater. 34 (2014) 106–115, https://doi.org/10.1016/j.jmbbm.2014.02.003.
[12] L. del-Mazo-Barbara, L. Johansson, F. Tampieri, M.P. Ginebra, Toughening 3D printed biomimetic hydroxyapatite scaffolds: polycaprolactone-based self-hardening inks, Acta Biomater. 177 (2024) 506–524, https://doi.org/10.1016/J.ACTBIO.2024.02.012.
[13] R. Pugliese, S. Graziosi, Biomimetic scaffolds using triply periodic minimal surface-based porous structures for biomedical applications, SLAS Technol. 28 (2023) 165–182, https://doi.org/10.1016/J.SLAST.2023.04.004.
[14] C.J. Culbreath, B. Gaerke, M.S. Taylor, S.D. McCullen, O.T. Mefford, Effect of infill on resulting mechanical properties of additive manufactured bioresorbable polymers for medical devices, Materialia (Oxf) 12 (2020) 100732, https://doi.org/10.1016/j.mtla.2020.100732.
[15] S.A.M. Tofail, E.P. Koumoulos, A. Bandyopadhyay, S. Bose, L. O'Donoghue, C. Charitidis, Additive manufacturing: scientific and technological challenges, market uptake and opportunities, Mater. Today 00 (2017) 1–16, https://doi.org/10.1016/j.mattod.2017.07.001.
[16] R. Pugliese, S. Graziosi, Biomimetic scaffolds using triply periodic minimal surface-based porous structures for biomedical applications, SLAS Technol. 28 (2023) 165–182, https://doi.org/10.1016/J.SLAST.2023.04.004.
[17] D.W. Abueidda, M. Elhebeary, C.S. Andrew Shiang, S. Pang, R.K. Abu Al-Rub, I. M. Jasiuk, Mechanical properties of 3D printed polymeric Gyroid cellular structures: experimental and finite element study, Mater. Des. 165 (2019) 107597, https://doi.org/10.1016/J.MATDES.2019.107597.
[18] E.A. Ramírez, N. Béraud, F. Pourroy, F. Villeneuve, M. Museau, Design parameters effects on relative density of triply periodic minimal surfaces for additive manufacturing, Procedia CIRP 100 (2021) 13–18, https://doi.org/10.1016/J.PROCIR.2021.05.002.
[19] K. Wang, H. Wang, J. Zhang, X. Fan, Mechanical behavior of interpenetrating phase composite structures based on triply periodic minimal surface lattices, Compos. Struct. 337 (2024) 118044, https://doi.org/10.1016/J.COMPSTRUCT.2024.118044.
[20] H. Jiang, A. Coomes, Z. Zhang, H. Ziegler, Y. Chen, Tailoring 3D printed graded architected polymer foams for enhanced energy absorption, Compos. B Eng. 224 (2021) 109183, https://doi.org/10.1016/j.compositesb.2021.109183.

[21] J. Plocher, A. Panesar, Effect of density and unit cell size grading on the stiffness and energy absorption of short fibre-reinforced functionally graded lattice structures, Addit. Manuf. 33 (2020) 101171, https://doi.org/10.1016/j.addma.2020.101171.
[22] M. Araya, M. Jaskari, T. Rautio, T. Guillén, A. Järvenpää, Assessing the compressive and tensile properties of TPMS-Gyroid and stochastic Ti64 lattice structures: a study on laser powder bed fusion manufacturing for biomedical implants, J. Sci. Adv. Mater. Dev. 9 (2024) 100663, https://doi.org/10.1016/j.jsamd.2023.100663.
[23] Y. Yang, G. Wang, H. Liang, C. Gao, S. Peng, L. Shen, C. Shuai, Additive manufacturing of bone scaffolds, Int. J. Bioprint. 5 (2019) 1–25, https://doi.org/10.18063/IJB.v5i1.148.
[24] E. Alabort, D. Barba, R.C. Reed, Design of metallic bone by additive manufacturing, Scr. Mater. 164 (2019) 110–114, https://doi.org/10.1016/j.scriptamat.2019.01.022.
[25] J. Van Erum, D. Van Dam, P.P. De Deyn, Additive manufacturing for bone tissue engineering scaffolds, Neurosci. Biobehav. Rev. (2019) 100632, https://doi.org/10.1016/j.neubiorev.2019.07.019.
[26] O.J. Aryeetey, L. Jaksa, M. Bittner-Frank, A. Lorenz, D.H. Pahr, Development of 3D printed tissue-mimicking materials: combining fiber reinforcement and fluid content for improved surgical rehearsal, Materialia (Oxf) 34 (2024) 102088, https://doi.org/10.1016/j.mtla.2024.102088.
[27] L. Yang, S. Wu, C. Yan, P. Chen, L. Zhang, C. Han, C. Cai, S. Wen, Y. Zhou, Y. Shi, Fatigue properties of Ti-6Al-4V Gyroid graded lattice structures fabricated by laser powder bed fusion with lateral loading, Addit. Manuf. 46 (2021) 102214, https://doi.org/10.1016/j.addma.2021.102214.
[28] J. Jin, S. Wu, L. Yang, C. Zhang, Y. Li, C. Cai, C. Yan, Y. Shi, Ni–Ti multicell interlacing Gyroid lattice structures with ultra-high hyperelastic response fabricated by laser powder bed fusion, Int. J. Mach. Tools. Manuf. 195 (2024) 104099, https://doi.org/10.1016/j.ijmachtools.2023.104099.
[29] F.S.L. Bobbert, K. Lietaert, A.A. Eftekhari, B. Pouran, S.M. Ahmadi, H. Weinans, A. A. Zadpoor, Additively manufactured metallic porous biomaterials based on minimal surfaces: a unique combination of topological, mechanical, and mass transport properties, Acta Biomater. 53 (2017) 572–584, https://doi.org/10.1016/j.actbio.2017.02.024.
[30] D. Barba, E. Alabort, R.C. Reed, Synthetic bone: design by additive manufacturing, Acta Biomater. 97 (2019) 637–656, https://doi.org/10.1016/j.actbio.2019.07.049.
[31] Y. Wu, J. Liu, L. Kang, J. Tian, X. Zhang, J. Hu, Y. Huang, F. Liu, H. Wang, Z. Wu, An overview of 3D printed metal implants in orthopedic applications: present and future perspectives, Heliyon 9 (2023) e17718, https://doi.org/10.1016/j.heliyon.2023.e17718.
[32] J. Li, D. Guo, J. Li, X. Wei, Z. Sun, B. Yang, T. Lu, P. Ouyang, S. Chang, W. Liu, X. He, Irregular pore size of degradable bioceramic Voronoi scaffolds prepared by stereolithography: osteogenesis and computational fluid dynamics analysis, Mater. Des. 224 (2022) 111414, https://doi.org/10.1016/J.MATDES.2022.111414.
[33] E. Frayssinet, L. Colabella, A.P. Cisilino, Design and assessment of the biomimetic capabilities of a Voronoi-based cancellous microstructure, J. Mech. Behav. Biomed. Mater. 130 (2022) 105186, https://doi.org/10.1016/J.JMBBM.2022.105186.
[34] X. Wang, S. Xu, S. Zhou, W. Xu, M. Leary, P. Choong, M. Qian, M. Brandt, Y. Min, Topological design and additive manufacturing of porous metals for bone scaffolds and orthopaedic implants : a review, Biomaterials 83 (2016), https://doi.org/10.1016/j.biomaterials.2016.01.012.
[35] H. Qi, J. Qi, J. Gao, J. Sun, G. Wang, The impact of bone mineral density on bone metabolism and the fracture healing process in elderly chinese patients with osteoporotic vertebral compression fractures, J. Clin. Densitometry 24 (2021) 135–145, https://doi.org/10.1016/J.JOCD.2020.11.003.
[36] D. Ke, J. Yu, P. Liu, C. Niu, X. Yang, Biomimetic 3D printed PCL/TCP/GelMA scaffolds with improved osteogenesis and angiogenesis for non-load bearing applications, Materialia (Oxf) 21 (2022) 101339, https://doi.org/10.1016/j.mtla.2022.101339.
[37] J.A. Gasser, M. Kneissel, Bone toxicology (2017), https://doi.org/10.1007/978-3-319-56192-9.
[38] L.J. Gibson, The mechanical behaviour of cancellous bone, J. Biomech. 18 (1985) 317–328, https://doi.org/10.1016/0021-9290(85)90287-8.
[39] D.W. Hutmacher, T. Schantz, I. Zein, K.W. Ng, S.H. Teoh, K.C. Tan, Mechanical properties and cell cultural response of polycaprolactone scaffolds designed and fabricated via fused deposition modeling, J. Biomed. Mater. Res. 55 (2001) 203–216. An Official Journal of The Society for Biomaterials, The Japanese Society for Biomaterials, and The Australian Society for Biomaterials and the Korean Society for Biomaterials.
[40] L.J. Gibson, Biomechanics of cellular solids, J. Biomech. 38 (2005) 377–399, https://doi.org/10.1016/j.jbiomech.2004.09.027.
[41] D. Zhao, H. Liang, C. Han, J. Li, J. Liu, K. Zhou, C. Yang, Q. Wei, 3D printing of a titanium-tantalum Gyroid scaffold with superb elastic admissible strain, bioactivity and in-situ bone regeneration capability, Addit. Manuf. 47 (2021) 102223, https://doi.org/10.1016/j.addma.2021.102223.
[42] S. Li, E. Demirci, V.V. Silberschmidt, Variability and anisotropy of mechanical behavior of cortical bone in tension and compression, J. Mech. Behav. Biomed. Mater. 21 (2013) 109–120, https://doi.org/10.1016/j.jmbbm.2013.02.021.
[43] G. Allen (n.d.), Field Driven Design, nTop. https://www.ntop.com/resources/guides/download-whitpaper-field-driven-design/.
[44] L.J. Gibson, Biomechanics of cellular solids, J. Biomech. 38 (2005) 377–399, https://doi.org/10.1016/j.jbiomech.2004.09.027.
[45] B. Hanks, J. Berthel, M. Frecker, T.W. Simpson, Mechanical properties of additively manufactured metal lattice structures: data review and design interface, Addit. Manuf. 35 (2020) 101301, https://doi.org/10.1016/j.addma.2020.101301.
[46] J. Deering, K. Grandfield, Current interpretations on the in vivo response of bone to additively manufactured metallic porous scaffolds: a review, Biomater. Biosyst. 2 (2021) 100013, https://doi.org/10.1016/j.bbiosy.2021.100013.
[47] H. Chen, Q. Han, C. Wang, Y. Liu, B. Chen, J. Wang, Porous Scaffold design for additive manufacturing in orthopedics: a review, Front. Bioeng. Biotechnol. 8 (2020), https://doi.org/10.3389/fbioe.2020.00609.
[48] S. Kechagias, R.N. Oosterbeek, M.J. Munford, S. Ghouse, J.R.T. Jeffers, Controlling the mechanical behaviour of stochastic lattice structures: the key role of nodal connectivity, Addit. Manuf. 54 (2022) 102730, https://doi.org/10.1016/j.addma.2022.102730.
[49] O. Al-Ketan, D.-W. Lee, R.K. Abu Al-Rub, Mechanical properties of additively-manufactured sheet-based gyroidal stochastic cellular materials, Addit. Manuf. 48 (2021) 102418, https://doi.org/10.1016/j.addma.2021.102418.
[50] S. Eshraghi, S. Das, Mechanical and microstructural properties of polycaprolactone scaffolds with one-dimensional, two-dimensional, and three-dimensional orthogonally oriented porous architectures produced by selective laser sintering, Acta Biomater. 6 (2010) 2467–2476, https://doi.org/10.1016/j.actbio.2010.02.002.
[51] D.W. Hutmacher, Scaffolds in tissue engineering bone and cartilage, Biomaterials 21 (2000) 2529–2543, https://doi.org/10.1016/S0142-9612(00)00121-6.
[52] A.D. Olubamiji, Z. Izadifar, J.L. Si, D.M.L. Cooper, B.F. Eames, D.X. Chen, Modulating mechanical behaviour of 3D-printed cartilage-mimetic PCL scaffolds: influence of molecular weight and pore geometry, Biofabrication 8 (2016) 025020, https://doi.org/10.1088/1758-5090/8/2/025020.
[53] Y. Li, C. Yang, H. Zhao, S. Qu, X. Li, Y. Li, New developments of Ti-based alloys for biomedical applications, Materials 7 (2014) 1709–1800, https://doi.org/10.3390/ma7031709.
[54] A. Paradowska-Stolarz, J. Wezgowiec, M. Mikulewicz, Comparison of two chosen 3D printing resins designed for orthodontic use: an in vitro study, Materials 16 (2023) 2237, https://doi.org/10.3390/ma16062237.
[55] A.M. Paradowska-Stolarz, M. Wieckiewicz, M. Mikulewicz, A. Malysa, I. Dus-Ilnicka, P. Seweryn, J. Laskowska, M.C. Figueiredo Pollamann, M. Adamska, J. Wezgowiec, Comparison of the tensile modulus of three 3D-printable materials used in dentistry, Dent. Med. Probl. 60 (2023) 505–511, https://doi.org/10.17219/dmp/166070.
[56] A. Paradowska-Stolarz, M. Mikulewicz, M. Wieckiewicz, J. Wezgowiec, The influence of polishing and artificial aging on BioMed Amber® Resin's mechanical properties, J. Funct. Biomater. 14 (2023) 254, https://doi.org/10.3390/jfb14050254.
[57] E. Schileo, F. Taddei, L. Cristofolini, M. Viceconti, Subject-specific finite element models implementing a maximum principal strain criterion are able to estimate failure risk and fracture location on human femurs tested in vitro, J. Biomech. 41 (2008) 356–367, https://doi.org/10.1016/j.jbiomech.2007.09.009.